Topology optimization of periodic lattice structures taking into account strain gradient

Daicong Da[a,b], Julien Yvonnet[b,*], Liang Xia[c], Minh Vuong Le[b], Guangyao Li[a,*]

[a]*State Key Laboratory of Advanced Design and Manufacturing for Vehicle Body,*
Hunan University, Changsha, China
[b]*Université Paris-Est, Laboratoire Modélisation et Simulation Multi Echelle MSME,*
UMR CNRS 8208, 5 bd Descartes, 77454 Marne-la-Vallée, France
[c]*State Key Laboratory of Digital Manufacturing Equipment and Technology,*
Huazhong University of Science and Technology, Wuhan, China

Abstract

We present a topology optimization for lattice structures in the case of non-separated scales, i.e. when the characteristic dimensions of the periodic unit cells in the lattice are not much smaller than the dimensions of the whole structure. The present method uses a coarse mesh corresponding to a homogenized medium taking into strain gradient through a non-local numerical homogenization method. Then, the topological optimization procedure only uses the values at the nodes of the coarse mesh, reducing drastically the computational times. We show that taking into account the strain gradient within the topological optimization procedure brings significant increase in the resulting stiffness of the optimized lattice structure when scales are not separated, as compared to using a homogenized model based on the scale separation assumption.

Keywords: Strain gradient, Non-separated scales, Lattice structures, Computational homogenization, Topology optimization, BESO

1. Introduction

Topological optimization of heterogeneous media has been an active research topic in the last decades and has become a subject of major importance with the growing development of additive manufacturing processes, which allow fabricating workpieces like lattice structures with arbitrary geometrical details (see a recent review in [1]). In that context, topology optimization [2, 3] aims to define the optimal structural or material geometry with regards to specific objectives (e.g. maximal stiffness, minimal mass, or maximizing other physical/mechanical properties), under mechanical constraints like equilibrium and boundary conditions.

---

[*]Corresponding author
  Email addresses: `julien.yvonnet@univ-paris-est.fr` (Julien Yvonnet), `gyli@hnu.edu.cn` (Guangyao Li)

Over the past decades, many methods have been proposed to solve topology optimization problems, including density-based methods [4, 5], evolutionary procedures [6–8], level-set methods [9–11], among others.

Initially restricted to optimizing the geometry of structures, the technique has been extended to optimizing the topology of the phase within materials, e.g. in periodic microstructures, to design high performance materials [12–20] or materials with properties not found in nature (negative Poisson's ratio, zero compressibility, negative bulk modulus, etc. (see [21–25]) or complex multi-physics problems [26, 27]. These techniques are based on optimizing the homogenized properties of the representative volume element, and using numerical solving methods like finite element to compute the homogenized properties [28], given one geometry of the phases and their microscopic properties. Recent extensions to nonlinear materials [29, 30], multiple phase materials [31] and resistance to fracture [32, 33] have been proposed recently.

In topology optimization applied to material modeling, the assumption of scale separation is often assumed. This assumption states that the characteristic length of the microstructural details are much smaller than the dimensions of the structure, or that the characteristic wavelength of the applied load is much larger than that of the local fluctuation of mechanical fields [34]. In additive manufacturing of architecture materials like lattice structures, the manufacturing process might induce limitations on the size of local details, which can lead to a violation of scale separation when the characteristic size of the periodic unit cells within the lattice are not much smaller than that of the structure. In such case, classical homogenization methods may lead to inaccurate description of the effective behavior as non local effects, or strain-gradient effects, may occur within the structure. On the other hand, using a fully detailed description of the lattice structure in a optimization framework could be computationally very costly.

In the present work, the objective is to develop a topology optimization procedure for heterogeneous materials such as lattice materials in a context of non-separated scales. The idea is to use a computational homogenization method which takes into account the strain gradient effects combined with a topological optimization scheme of unit cells, allowing the topological optimization problem to be performed on a coarse mesh, instead of using the fully detailed description of the structure for computational saving.

Whereas several computational homogenization methods taking into account strain gradient effects are available (see e.g. [35–37]), we have used the technique developed in [38–40]. The major advantage of this technique is that it can take into account an arbitrary level of strain gradient without higher order elements, in a classical finite element framework. The technique generalizes the homogenization theory by replacing spatial averaging operators by linear low-pass filters. For self-consistency of the paper, the technique is reviewed in section 2. The used topological optimization method is based on the bi-directional evolutionary structural optimization (BESO) technique [41], due to its simplicity.

Other studies have been devoted to topology optimization of structures in a context of non-separated scales (see e.g. [42–45]. However, to our best knowledge, the present work is the first to take into account the effects of strain gradient in the topology optimization through an appropriate homogenization scheme combined with the topology optimization strategy.

The remainder of the paper is organized as follows. A review of the computational homogenization used to take into account the strain gradient effects based on numerical filters is provided

in section 2. The procedure combining this homogenization method with the topological optimization procedure is described in section 3. The homogenization method is validated in section 4 and the proposed methodology is applied to lattice structures in section 5 to study the gain of taking into account the strain gradient effects as compared to a topology optimization combined with classical homogenization in a context of non-separated scales.

2. Nonlocal filter-based homogenization for non-separated scales

2.1. Definition of local and mesoscopic fields through the filter

In this section, we first briefly review the homogenization method that we use to take into account strain gradient effects. The method, called filter-based homogenization method, was introduced in [38] and later extended in [39, 40]. The main idea is to construct a mesoscopic non local homogenized model using computations on the Representative Volume Element (RVE) by replacing averaging operators in the homogenization theory by linear numerical filters. In this framework, a convenient numerical model based on a coarse mesh of the heterogeneous structure can be constructed, while keeping the possibility of re-localizing all microstructural mechanical fields.

We consider two scales, one called microscopic scale, associated to fine scale strain and stress fields $\boldsymbol{\varepsilon}(\boldsymbol{x})$ and $\boldsymbol{\sigma}(\boldsymbol{x})$, and another one called *mesoscopic scale*, associated to strain and stress fields at the upper scale, denoted by $\hat{\boldsymbol{\varepsilon}}(\boldsymbol{x})$ and $\hat{\boldsymbol{\sigma}}(\boldsymbol{x})$. Note that the *mesoscopic* fields have a characteristic wavelength which is not necessarily much larger than that of the microscopic fluctuations fields. As illustrated in Fig. 1, structures considered in the present work are assumed to be composed of periodic substructures or unit cells. The length scale of microscopic unit cell is comparable to the structural length scale such that the scale separation cannot be assumed. A coarse mesh is associated with the whole structure, and each substructure/unit cell is meshed with the same number of coarse elements. In addition, the microscopic structure (unit cell) is meshed using a fine mesh related to the microscopic scale. The mesoscopic strain and stress fields $\hat{\boldsymbol{\varepsilon}}$ and $\hat{\boldsymbol{\sigma}}$ are then approximated on the coarse mesh (see Fig. 1(a)), whereas the microscopic fields $\boldsymbol{\varepsilon}$ and $\boldsymbol{\sigma}$ are evaluated on the fine mesh (see Fig. 1(b)). The size of the fine grid is assumed to be small enough to catch all the fluctuations of the microstructure at the smallest scale.

Mesoscopic and microscopic fields are related by:

$$\begin{cases} \hat{\boldsymbol{\varepsilon}} = \mathcal{F}\{\boldsymbol{\varepsilon}(\boldsymbol{x})\}, \\ \hat{\boldsymbol{\sigma}} = \mathcal{F}\{\boldsymbol{\sigma}(\boldsymbol{x})\}, \end{cases} \tag{1}$$

where $\mathcal{F}$ is a linear operator, acting as a low-pass filter on the fine scale fluctuations. This operator is associated to a characteristic length h related to the field fluctuations observed at the mesoscopic scale. In order to construct a theory able to describe continuously mesoscopic fields from the microscale up to the macroscale, and precisely overcome the limitations of scale separation, the
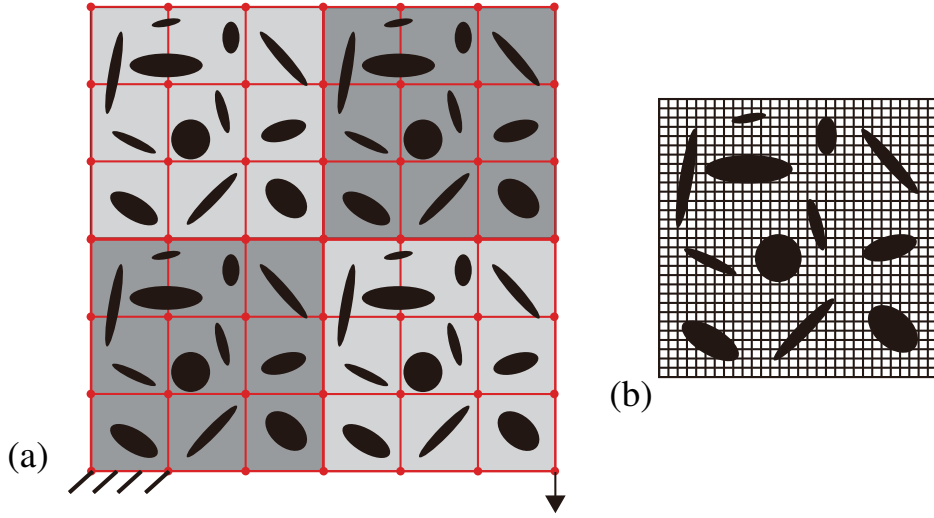
Figure 1: (a) Coarse mesh covering the structure and unit cells; (b) Fine mesh over the unit cell.

following properties are required for the filter [38–40]:

$$
\begin{cases}
\lim_{h\to 0} \mathcal{F}\{h, \varepsilon(\boldsymbol{x})\} = \varepsilon(\boldsymbol{x}), \\
\lim_{h\to \infty} \mathcal{F}\{h, \varepsilon(\boldsymbol{x})\} = \langle\varepsilon(\boldsymbol{x})\rangle, \\
\mathcal{F}\{\mathcal{F}\{\varepsilon(\boldsymbol{x})\}\} = \mathcal{F}\{\varepsilon(\boldsymbol{x})\},
\end{cases}
\tag{2}
$$

where $\langle.\rangle$ denotes averaging operator.

A least-square polynomial filter introduced in [39], which consists of in a least-square projection of the microscopic strain field over a piece-wise polynomial basis, is adopted in this work. By this filter process, the mesoscopic fields are expressed as

$$
\begin{cases}
\hat{\varepsilon}_{ij}(\boldsymbol{x}) = \sum_{p=1}^{P} M^p(\boldsymbol{x})\hat{\varepsilon}_{ij}^p, \\
\hat{\sigma}_{ij}(\boldsymbol{x}) = \sum_{p=1}^{P} M^p(\boldsymbol{x})\hat{\sigma}_{ij}^p,
\end{cases}
\tag{3}
$$

where $M^p(\boldsymbol{x})$ are piece-wise polynomial basis functions (e.g. finite element shape functions) to nodes $p, p = 1, ..., P$ of a coarse mesh covering the domain where the microscopic fields are described. Given the fine scale strain field on a discrete fine mesh composed of N nodes $\boldsymbol{x}^m, m = 1, 2, ..., N$, the unknown coefficients $\hat{\varepsilon}_{ij}^p$ are required to minimize the distance between the approximation and the given fine scale strain field in the least-square sense. Let us define U such that

$$
U = \sum_{m=1}^{N} \left(\sum_{p=1}^{P} M^p(\boldsymbol{x}^m)\hat{\varepsilon}_{ij}^p - \varepsilon_{ij}(\boldsymbol{x}^m) \right)^2.
\tag{4}
$$

Optimality conditions give

$$
\frac{dU}{d\hat{\varepsilon}_{ij}^q} = 0, \quad q = 1, 2, ..., N,
\tag{5}
$$

4

leading to

$$2 \sum_{m=1}^{N} M^q(\boldsymbol{x^m})(\sum_{p=1}^{P} M^p(\boldsymbol{x^m})\hat{\varepsilon}_{ij}^p - \varepsilon_i j(\boldsymbol{x^m})) = 0, \quad q = 1, 2, .., N, \tag{6}$$

or

$$\sum_{p=1}^{P} \left(\sum_{m=1}^{N} M^p(\boldsymbol{x^m})M^q(\boldsymbol{x^m}) \right) \hat{\varepsilon}_{ij}^p = \sum_{m=1}^{N} M^q(\boldsymbol{x^m})\varepsilon_{ij}(\boldsymbol{x^m}). \tag{7}$$

Then the coefficients ε_{ij}^p, $p = 1, 2, ..., N$ are found by solving the following system:

$$A\mathrm{u} = \boldsymbol{b}, \tag{8}$$

where

$$A_{pq} = \sum_{m=1}^{N} M^p(\boldsymbol{x^m})M^q(\boldsymbol{x^m}), \quad b_q = \sum_{m=1}^{N} M^p(\boldsymbol{x^m})\varepsilon_{ij}(\boldsymbol{x^m}), \tag{9}$$

and where $\mathrm{u} = [\hat{\varepsilon}_{ij}^1, \hat{\varepsilon}_{ij}^2, ..., \hat{\varepsilon}_{ij}^N]$.

2.2. Microscopic unit cell calculations

2.2.1. Local problem

Let us consider a unit cell $\Omega \subset \mathbb{R}^d$ as defined in Section 2.1, d being the dimension of the space, with boundary $\partial\Omega$. The unit cell is related to microscopic scale where the fields are described at the finest scale. The local problem on the unit cell for non-separated scales is defined as follows: assuming known an applied non-constant mesoscopic strain field $\hat{\boldsymbol{\varepsilon}}(\boldsymbol{x})$, find $\boldsymbol{\varepsilon}(\boldsymbol{x})$ satisfying;

$$\nabla \cdot (\boldsymbol{\sigma}(\boldsymbol{x})) = 0 \quad \text{in } \Omega \tag{10}$$

and

$$\boldsymbol{\sigma}(\boldsymbol{x}) = \mathbb{C}(\boldsymbol{x}) : \boldsymbol{\varepsilon}(\boldsymbol{x}), \tag{11}$$

with

$$\mathcal{F}\{\boldsymbol{\varepsilon}(\boldsymbol{x})\} = \hat{\boldsymbol{\varepsilon}}(\boldsymbol{x}) \quad \text{in } \Omega, \tag{12}$$

where $\mathbb{C}(\boldsymbol{x})$ is a fourth-order elasticity tensor, and $\nabla\cdot(.)$ denotes the divergence operator. Instead of requiring that the spatial average of the strain fields matches the mesoscopic one as in the classical homogenization, the introduced condition (12) states that the filtered part of the compatible strain field must match the given non-uniform mesoscopic strain field $\hat{\boldsymbol{\varepsilon}}(\boldsymbol{x})$. This problem is then different from the local problem in classical homogenization.

Following [38], the microscopic strain field is split into a filtered (mesoscopic) part and a remaining fluctuation $\tilde{\boldsymbol{\varepsilon}}(\boldsymbol{x})$:

$$\boldsymbol{\varepsilon}(\boldsymbol{x}) = \hat{\boldsymbol{\varepsilon}}(\boldsymbol{x}) + \tilde{\boldsymbol{\varepsilon}}(\boldsymbol{x}). \tag{13}$$

Introducing (11) and (13) into (10) and using the property (2)(c), the new localization problem is obtained as:

$$\nabla \cdot (\mathbb{C}(\boldsymbol{x}) : \tilde{\boldsymbol{\varepsilon}}(\boldsymbol{x})) = -\nabla \cdot (\mathbb{C}(\boldsymbol{x}) : \hat{\boldsymbol{\varepsilon}}(\boldsymbol{x})) \quad \text{in } \Omega \tag{14}$$

with

$$\mathcal{F}\{\tilde{\varepsilon}(\boldsymbol{x})\} = 0 \quad \text{in } \Omega. \tag{15}$$

To enforce the non-trivial condition (12), an auxiliary strain field $e(x)$ is defined by $\tilde{\varepsilon}(\boldsymbol{x}) = \boldsymbol{e}(\boldsymbol{x}) - \mathcal{F}(\boldsymbol{e}(\boldsymbol{x}))$. Invoking again the property (2)(c), we have:

$$\mathcal{F}\{\tilde{\varepsilon}(\boldsymbol{x})\} = \mathcal{F}\{\boldsymbol{e}(\boldsymbol{x}) - \mathcal{F}\{\boldsymbol{e}(\boldsymbol{x})\}\} = \mathcal{F}\{\boldsymbol{e}(\boldsymbol{x})\} - \mathcal{F}\{\mathcal{F}\{\boldsymbol{e}(\boldsymbol{x})\}\} = 0. \tag{16}$$

The new local problem (14) then can be re-written by seeking $\boldsymbol{e}(\boldsymbol{x})$ satisfying

$$\nabla \cdot (\mathbb{C}(\boldsymbol{x}) : [\boldsymbol{e}(\boldsymbol{x}) - \mathcal{F}\{\boldsymbol{e}(\boldsymbol{x})\}]) = -\nabla \cdot (\mathbb{C}(\boldsymbol{x}) : \hat{\varepsilon}(\boldsymbol{x})) \quad \text{in } \Omega. \tag{17}$$

Condition (15) implies that

$$\langle \tilde{\varepsilon}(\boldsymbol{x}) \rangle = 0 \tag{18}$$

which is satisfied for any value of the spatial average $\langle \boldsymbol{e}(\boldsymbol{x}) \rangle$. So, we choose $\langle \boldsymbol{e}(\boldsymbol{x}) \rangle = 0$, and this equation is classically verified for the two possible sets of boundary conditions:

$$\boldsymbol{u}^e(\boldsymbol{x}) = 0 \quad \text{on } \partial\Omega, \tag{19}$$

or

$$\boldsymbol{u}^e(\boldsymbol{x}) = 0 \quad \text{periodic on } \partial\Omega, \tag{20}$$

where $\boldsymbol{u}^e$ is a compatible displacement field such that $\boldsymbol{e}(\boldsymbol{x}) = \boldsymbol{\varepsilon}(\boldsymbol{u}^e(\boldsymbol{x}))$, with $\boldsymbol{\varepsilon}(.) = \frac{1}{2}(\nabla(.) + \nabla^T(.))$.

To summarize, the new problem is defined by Eq.(14) with boundary conditions (19) or (20). In the present work, the first set of boundary conditions is adopted. The presence of the nonlocal operator in the left-hand term of (17) introduces a numerical difficulty, as the stiffness matrix associated with this linear operator is fully populated. Following [39, 40], the following iterative scheme is defined to alleviate this difficulty: starting from an initialized solution $\boldsymbol{e}^0(\boldsymbol{x})$, e.g. $\boldsymbol{e}^0(\boldsymbol{x}) = 0$, we seek the sought field $\boldsymbol{e}^{n+1}(\boldsymbol{x})$ at each iteration n of the following scheme:

$$\nabla \cdot (\mathbb{C}(\boldsymbol{x}) : \boldsymbol{e}^{n+1}(\boldsymbol{x})) = \nabla \cdot (\mathbb{C}(\boldsymbol{x}) : \mathcal{F}\{\boldsymbol{e}^n(\boldsymbol{x})\} - \nabla \cdot (\mathbb{C}(\boldsymbol{x}) : \hat{\varepsilon}(\boldsymbol{x})) \tag{21}$$

until a convergence criterion is reached. At convergence, the strain field is recovered as follows:

$$\boldsymbol{\varepsilon}(\boldsymbol{x}) = \hat{\varepsilon}(\boldsymbol{x}) + \boldsymbol{e}^{n+1}(\boldsymbol{x}) - \mathcal{F}\{\boldsymbol{e}^{n+1}(\boldsymbol{x})\}. \tag{22}$$

2.2.2. Discrete formulation

Following [40], we assume that the mesoscopic strain field derives from a mesoscopic displacement field $\hat{\boldsymbol{u}}(\boldsymbol{x})$ related to the mesoscopic scale as follows:

$$\hat{\varepsilon}_{ij}(\boldsymbol{x}) = \frac{1}{2}\left(\frac{\partial \hat{u}_i(\boldsymbol{x})}{\partial x_j} + \frac{\partial \hat{u}_j(\boldsymbol{x})}{\partial x_i}\right). \tag{23}$$

The mesoscopic displacement field is interpolated on the coarse mesh by finite element shape functions as:

$$\hat{u}_i(\boldsymbol{x}) \simeq \sum_p M^p(\boldsymbol{x})\hat{u}_i^p, \tag{24}$$

6

where $M^p(\mathbf{x})$ is the finite element shape function associated with the node p and $\hat{u}_i^p$ are the nodal components of $\hat{\mathbf{u}}(\mathbf{x})$ on the coarse mesh. Then, the corresponding strain field is given by:

$$\hat{\varepsilon}_{ij}(\mathbf{x}) \simeq \sum_{p=1}^{P} \frac{1}{2}\left(\frac{\partial M^p(\mathbf{x})}{\partial x_j}\hat{u}_i^p + \frac{\partial M^p(\mathbf{x})}{\partial x_i}\hat{u}_j^p\right), \tag{25}$$

where P is the number of nodes on the coarse mesh of the unit cell. This equation can be re-written as:

$$\hat{\varepsilon}_{ij}(\mathbf{x}) \simeq \sum_{p=1}^{P} \frac{1}{2}\left(\frac{\partial M^p(\mathbf{x})}{\partial x_j}\delta_{ik} + \frac{\partial M^p(\mathbf{x})}{\partial x_i}\delta_{jk}\right)\hat{u}_k^p. \tag{26}$$

From the superposition principle, the solution of the local problem is then a linear combination of the components of nodal displacements components $\hat{u}_k^p$ on the coarse mesh:

$$\varepsilon_{ij}(\mathbf{x}) \simeq \sum_{p=1}^{P} \mathcal{D}_{ijk}^p(\mathbf{x})\hat{u}_k^p. \tag{27}$$

Introducing the vector forms for the second-order tensors $\boldsymbol{\varepsilon}$ and $\boldsymbol{\sigma}$: $[\boldsymbol{\varepsilon}] = [\varepsilon_{11}, \varepsilon_{22}, 2\varepsilon_{12}]^T$, $[\boldsymbol{\sigma}] = [\sigma_{11}, \sigma_{22}, \sigma_{12}]^T$, Eq. (27) can be re-written into the matrix form in 2D as follows:

$$[\boldsymbol{\varepsilon}](\mathbf{x}) = \sum_p \begin{bmatrix} D_{11}^p(\mathbf{x}) & D_{12}^p(\mathbf{x}) \\ D_{21}^p(\mathbf{x}) & D_{22}^p(\mathbf{x}) \\ D_{31}^p(\mathbf{x}) & D_{32}^p(\mathbf{x}) \end{bmatrix}\begin{bmatrix} \hat{u}_1^p \\ \hat{u}_2^p \end{bmatrix}, \tag{28}$$

where the column $[D_{11}^p(\mathbf{x}), D_{21}^p(\mathbf{x}), D_{31}^p(\mathbf{x})]$ is the strain vector obtained from solving the local problem with $\hat{\boldsymbol{\varepsilon}}(\mathbf{x})$ given by the expression (26) with $\hat{u}_1^p = 1$ and $\hat{u}_2^p = 0$. The column $[D_{12}^p(\mathbf{x}), D_{22}^p(\mathbf{x}), D_{32}^p(\mathbf{x})]$ is the strain vector obtained from solving the local problem with $\hat{\boldsymbol{\varepsilon}}(\mathbf{x})$ given by the expression (26) with $\hat{u}_1^p = 0$ and $\hat{u}_2^p = 1$. We show how to compute the $\mathbf{D}^p(\mathbf{x})$ in the following.

The corresponding weak form of the localization problem expressed in (21) can be formulated as: find $\mathbf{u}(\mathbf{x})$ satisfying periodic boundary condition (19), such that $\forall \delta\mathbf{u} \in H^1(\Omega)$:

$$\int_{\Omega} \boldsymbol{\varepsilon}\left([\mathbf{u}^e]^{n+1}\right) : \mathbf{C}(\mathbf{x}) : \boldsymbol{\varepsilon}(\delta\mathbf{u}(\mathbf{x}))d\Omega =$$

$$\int_{\Omega} \mathcal{F}\left\{\boldsymbol{\varepsilon}\left([\mathbf{u}^e]^{n+1}(\mathbf{x})\right)\right\} : \mathbf{C}(\mathbf{x}) : \boldsymbol{\varepsilon}(\delta\mathbf{u}(\mathbf{x}))d\Omega - \int_{\Omega} \hat{\boldsymbol{\varepsilon}}(\mathbf{x}) : \mathbf{C}(\mathbf{x}) : \boldsymbol{\varepsilon}(\delta\mathbf{u}(\mathbf{x}))d\Omega, \tag{29}$$

where $H^1(\Omega)$ is the usual Sobolev space. Using a classical FEM discretization over the fine mesh, we have:

$$\mathbf{K}\mathbf{U}^{n+1} = \mathbf{f}^n + \hat{\mathbf{f}}, \tag{30}$$

with

$$\mathbf{K} = \int_{\Omega} \mathbf{B}^T(\mathbf{x})\mathbf{C}(\mathbf{x})\mathbf{B}(\mathbf{x})d\Omega, \tag{31}$$

where $\mathbf{B}$ denotes the matrix of shape function derivatives, $\mathbf{C}$ is the matrix form associated with the fourth-order tensor $\mathbb{C}(\mathbf{x})$ in (11) and $\hat{\mathbf{f}}$ is the body force vector associated to the prescribed

non-uniform strain $\hat{\varepsilon}(\boldsymbol{x})$, which corresponds to an unitary displacement of one node of the coarse mesh as follows:

$$\hat{\mathbf{f}} = - \int_{\Omega} \mathbf{B}^T(\boldsymbol{x})\mathbf{C}(\boldsymbol{x})[\hat{\varepsilon}(\boldsymbol{x})]d\Omega \tag{32}$$

where $[\hat{\varepsilon}(\boldsymbol{x})]$ is the vector form associated with $\hat{\varepsilon}(\boldsymbol{x})$ and

$$\mathbf{f}^n = \int_{\Omega} \mathbf{B}^T(\boldsymbol{x})\mathbf{C}(\boldsymbol{x}) \left[\mathcal{F} \left\{ \varepsilon \left([\boldsymbol{u}^e]^n(\boldsymbol{x})\right) \right\} \right] d\Omega. \tag{33}$$

Note that in all $2 \times P$ problems as well as for all iterations of the iterative procedure, the same stiffness matrix $\mathbf{K}$ is involved, which then only needs to be computed and decomposed once. Finally, we obtain:

$$\begin{bmatrix} D_{11}^p(\boldsymbol{x}) & D_{12}^p(\boldsymbol{x}) \\ D_{21}^p(\boldsymbol{x}) & D_{22}^p(\boldsymbol{x}) \\ D_{31}^p(\boldsymbol{x}) & D_{32}^p(\boldsymbol{x}) \end{bmatrix} = \begin{bmatrix} \varepsilon_{11}^{(1)}(\boldsymbol{x}) & \varepsilon_{11}^{(2)}(\boldsymbol{x}) \\ \varepsilon_{22}^{(1)}(\boldsymbol{x}) & \varepsilon_{22}^{(2)}(\boldsymbol{x}) \\ \varepsilon_{12}^{(1)}(\boldsymbol{x}) & \varepsilon_{12}^{(2)}(\boldsymbol{x}) \end{bmatrix}. \tag{34}$$

Then, we have the following relationships:

$$[\varepsilon(\boldsymbol{x})] = \sum_{p=1}^{P} \mathbf{D}^p(\boldsymbol{x})\hat{\mathbf{u}}^p, \tag{35}$$

$$[\sigma(\boldsymbol{x})] = \sum_{p=1}^{P} \mathbf{C}(\boldsymbol{x})\mathbf{D}^p(\boldsymbol{x})\hat{\mathbf{u}}^p. \tag{36}$$

Applying the linear filter $\mathcal{F}$, we have

$$[\hat{\sigma}(\boldsymbol{x})] = \sum_{p} \hat{\mathbf{G}}^p(\boldsymbol{x})\hat{\mathbf{u}}^p, \tag{37}$$

with

$$\hat{\mathbf{G}}^p(\boldsymbol{x}) = \mathcal{F}\{\mathbf{C}(\boldsymbol{x})\mathbf{D}^p(\boldsymbol{x})\}. \tag{38}$$

As a result, the obtained constitutive relationship at the mesoscopic scale has been derived by a fully microscopically-based framework without any empirical assumptions. A simple and classical displacement-based finite element strategy is adopted to implement the numerical scheme without requiring any higher-order elements.

2.2.3. Computational procedure

The overall algorithm for the microscopic unit cell computations is summarized as follows:
For each point p of the coarse mesh covering the unit cell:

1. Solve the local problem (17) with boundary conditions (19) by using the FEM discretization over the fine mesh until convergence is reached.
2. Compute microscopic strain field $\varepsilon(\boldsymbol{x})$ using (22).
3. Compute $\mathbf{D}^p(\mathbf{x})$ using (34) and store it.

8

4. Compute $\hat{\mathbf{G}}^p(\boldsymbol{x})$ using (38) and store it. Only nodal values of $\hat{\mathbf{G}}^p(\boldsymbol{x})$ at the nodes of the coarse mesh need to be stored. The full spatial description in the unit cell can be recovered through finite element shape functions as: $\hat{\mathbf{G}}^p(\boldsymbol{x}) = \sum_i M^i(\boldsymbol{x})[\hat{\mathbf{G}}^p]_i$, where $[\hat{\mathbf{G}}^p]_i$ are the nodal values of $\hat{\mathbf{G}}^p(\boldsymbol{x})$ on the coarse mesh.

Once these tensors computed and stored, for an arbitrary distribution of nodal values of the mesoscopic displacement field $\hat{\mathbf{u}}^p$ over the coarse mesh, we can compute:

1. The reconstructed local stress field $\sigma(\boldsymbol{x})$ using (36).
2. The mesoscopic stress field $\hat{\sigma}(\boldsymbol{x})$ using (37)-(38).

2.3. Mesoscopic structure calculations

2.3.1. Mesoscopic problem

Let us consider a mesoscopic structure defined in a domain $\hat{\Omega} \subset \mathbb{R}^d$ with boundary $\partial\hat{\Omega}$. The structure is associated to the mesoscopic scale, that is, the strain and stress fields are described at the characteristic wavelength associated to the filter $\mathcal{F}$ allowing to define it on the coarse mesh. The structure is subdivided into periodic substructures corresponding to unit cells $\Omega^k (k = 1, ..., N_s)$, with N_s the number of substructures, as depicted in Fig. 1. The boundary $\partial\hat{\Omega}$ is composed of Dirichlet and Neumann parts, denoted respectively $\partial\hat{\Omega}_u$ and $\partial\hat{\Omega}_t$, where the displacements and tractions are prescribed.

The equilibrium equation is expressed by

$$\nabla \cdot (\hat{\sigma}(\boldsymbol{x})) + \hat{\mathbf{f}} = 0 \quad \text{in } \hat{\Omega} \tag{39}$$

with boundary conditions as:

$$\hat{\mathbf{u}}(\boldsymbol{x}) = \mathbf{u}^d \quad \text{on } \partial\hat{\Omega}_u \tag{40}$$

and

$$\hat{\sigma} \cdot \mathbf{n} = \mathbf{f}^d \quad \text{on } \partial\hat{\Omega}_t \tag{41}$$

completed with the mesoscopic constitutive law (37)-(38), where $\mathbf{u}^d$ and $\mathbf{f}^d$ are respectively the prescribed displacement and forces, and $\mathbf{n}$ denotes the external normal vector.

2.3.2. Discrete formulation

The weak form corresponding to the mesoscopic problem (39)-(41) is given as follows: find $\hat{\mathbf{u}} \in H^1(\Omega)$ satisfying the boundary condition (40) such that

$$\int_{\hat{\Omega}} [\hat{\sigma}(\hat{\mathbf{u}})] \cdot [\hat{\varepsilon}(\delta\hat{\mathbf{u}})] d\Omega = \int_{\partial\hat{\Omega}_t} \hat{\mathbf{F}} \cdot \delta\hat{\mathbf{u}} d\Gamma + \int_{\hat{\Omega}} \hat{\mathbf{f}} \cdot \delta\hat{\mathbf{u}} d\Omega = \delta\hat{W}^{ext} \tag{42}$$

where $\delta\hat{W}^{ext}$ denotes the variational strain energy. $\hat{\varepsilon}(\delta\hat{\mathbf{u}})$ is approximated on the coarse mesh using classical FEM shape functions

$$[\hat{\varepsilon}](\delta\hat{\mathbf{u}}) = \mathbf{B}\delta\hat{\mathbf{u}}^e \tag{43}$$

and $\delta\hat{\mathbf{u}}^e$ are nodal values of $\delta\hat{\mathbf{u}}$ on the coarse mesh. Then we have

$$\sum_k \int_{\hat{\Omega}^k} \sum_{p \in \hat{\Omega}^k} \hat{\mathbf{G}}^p(\boldsymbol{x})\hat{\mathbf{u}}^p \cdot \mathbf{B}(\boldsymbol{x})\delta\hat{\mathbf{u}}^e d\Omega = \delta\hat{W}^{ext}, \tag{44}$$

9

which leads to the linear system of equations

$$\hat{\mathbf{K}}\hat{\mathbf{u}} = \hat{\mathbf{F}} \tag{45}$$

with

$$\hat{\mathbf{K}} = \sum_k \sum_{p \in \hat{\Omega}^k} \int_{\hat{\Omega}^k} \mathbf{B}^T(\boldsymbol{x})\hat{\mathbf{G}}^p(\boldsymbol{x})d\Omega \tag{46}$$

and

$$\hat{\mathbf{F}} = \int_{\partial\hat{\Omega}} \mathbf{N}^T \cdot \hat{\mathbf{f}}d\Omega + \int_{\partial\hat{\Omega}_t} \mathbf{N}^T \cdot \bar{\mathbf{F}}d\Gamma. \tag{47}$$

where $\mathbf{N}$ denotes the shape function matrix.

The mesoscopic problem can be solved on a coarse mesh only, but the technique can provide all re-localized fine scale fields in the heterogeneous structure, as described in Section 2.2.

3. Topology optimization procedure

3.1. Model definition and sensitivity numbers

In this section, the BESO method [41] for topology optimization is extended to strain gradient effects by incorporating the non-local model presented in the previous section, and applied to lattice structures composed of periodic unit cells. Then, the topology of all unit cells is the same, but takes into account the response of the whole structure to maximize its stiffness. The structural stiffness maximization problem can be formulated using the design variable $\rho_e^{(k)}$, where k and e denote the substructure number and the element number in each substructure, respectively, as

$$
\begin{aligned}
\min_{\{\boldsymbol{\rho}^{(1)},\dots,\boldsymbol{\rho}^{(N_s)}\}} \quad &: \quad f_{\mathrm{c}}(\boldsymbol{\rho}, \hat{\mathbf{u}}) = \hat{\mathbf{F}}^T \hat{\mathbf{u}} \\
\text{subject to} \quad &: \quad \hat{\mathbf{K}}\hat{\mathbf{u}} = \hat{\mathbf{F}}, \\
& \quad V(\boldsymbol{\rho}) = N_s \sum \rho_e^{(k)} v_e^{(k)} = V_{\mathrm{req}}, \\
& \quad \rho_e^{(1)} = \cdots = \rho_e^{(N_s)}, \ e = 1,\dots,N_e, \\
& \quad \rho_e^{(k)} = \rho_{min} \text{ or } 1, \ e = 1,\dots,N_e,
\end{aligned} \tag{48}
$$

where f_{c} is known as the compliance functional, and $\hat{\mathbf{F}}$ and $\hat{\mathbf{u}}$ are respectively the applied load and displacement vectors defined at the mesoscopic scale in section 2.3.2. The above stiffness matrix $\hat{\mathbf{K}}$ is assembled by using the tensor $\hat{\mathbf{G}}^p$ defined in (46), where $\hat{\mathbf{G}}^p$ is obtained using (38). It should be noted that the computation of tensors $\hat{\mathbf{G}}^p$ and $\hat{\mathbf{D}}^p$ in (38) are both based on a fully microscopic framework accounting all heterogeneities at the microscale.

In (48), $v_e^{(k)}$ is the volume of the e−th element in the k−th unit cell, and N_e is the number of elements in the microscale fine mesh for each substructure. The condition $\rho_e^{(1)} = \cdots = \rho_e^{(N_s)}$ ensures that the pseudo densities (ρ_{min} or 1) of elements at the corresponding locations in each substructure are the same. During the process of evolutionary-type structural optimization, the elements are removed or added based on their sensitivity numbers. Therefore, the elements at the same locations in different substructures are removed or added simultaneously. However, the strain/stress distribution in different substructures/microscopic unit cells may not be the same in most cases.

10

To enforce the periodic array of the microscopic unit cells, the element sensitivity numbers at the same location in each unit cell need to be consistent. They are then defined as the summation of the sensitivity of corresponding elements in all unit cells. In conventional evolutionary structural optimization methods (see e.g., [41] and [46]), the element sensitivity number is defined as the change of the structural compliance or total strain energy since the removal of that element which is equal to the elemental strain energy. Therefore, the elemental sensitivity number in this scheme can be expressed as the variation of the overall structural compliance due to the removal of $e-$th elements in all substructures:

$$\alpha_e = \begin{cases} \sum_{k=1}^{N_s} \int_{\Omega_e^k} \sigma(x) \varepsilon(x) d\Omega_e^k, & \text{for } \rho_e^{(k)} = 1 \\ 0, & \text{for } \rho_e^{(k)} = \rho_{min}, \end{cases} \tag{49}$$

where σ and ε are respectively microscopic stress and strain fields in the $e-$th element of the $k-$th substructure Ω_e^k, which are evaluated directly from the obtained mesoscopic displacement field on the coarse mesh as formulated in section 2. By the presented nonlocal homogenization scheme, the re-localized strain and stress fields are obtained using (35) and (36).

Then, only computations on the coarse mesh are required, but all local fields can be reconstructed. This is highly advantageous to reduce the computational costs in the topology optimization procedure, which then only uses the coarse mesh nodal values of displacements.

3.2. Sensitivity modification and update scheme

To avoid the common issue of a checkerboard pattern in topology optimization, the above formulated sensitivity numbers are firstly smoothed by means of a filtering scheme [47]

$$\alpha_e = \frac{\sum_{j=1}^{N_e} w_{ej} \alpha_j}{\sum_{j=1}^{N_e} w_{ej}}, \tag{50}$$

where w_{ej} is a linear weight factor defined as:

$$w_{ej} = \max(0, r_{\min} - \Delta(e, j)), \tag{51}$$

determined according to the prescribed filter radius $r_{\min}$ and the element center-to-center distance $\Delta(e, j)$ between elements i and j. Due to the discrete nature of design variables (solid ($\rho_i = 1$) or void phase ($\rho_i = \rho_{min}$)) in the BESO method, the current sensitivity numbers are further smoothed along the evolution history to avoid spurious oscillations [41] as:

$$\alpha_e^{(iter)} = \frac{(\alpha_e^{(iter)} + \alpha_e^{(iter-1)})}{2}, \tag{52}$$

where *iter* is the current iteration number, thus, the updated sensitivity number includes all sensitivity information in the previous iterations.

With the modified sensitivity information, the considered structure can be tailored together with the target material volume at the current iteration $V_{(iter)}$. The target material volume can be predetermined as

$$V_{(iter)} = \max \left\{ V_{\text{req}}, (1 - c_{\text{er}}) V_{(iter-1)} \right\}, \tag{53}$$

11

where c_{er} is an evolutionary volume ratio which can be set by the designer to determine the amount of material to be removed from the previous design iteration. Once the volume constraint of the solid material V_{req} is reached, the volume is kept constant to the prescribed value.

The optimization procedure iteratively conducts the multiscale computations to determinate the sensitivity numbers and the update of topology in one substructure/unit cell until the volume constraint V_{req} is reached and the following convergence criterion is satisfied:

$$\frac{|\sum_{q=1}^{Q}\left(\Phi_{iter-q+1} - \Phi_{iter-Q-q+1}\right)|}{\sum_{q=1}^{Q}\Phi_{iter-q+1}} \leq \tau. \tag{54}$$

In the above, Φ denotes objective function, Q is the integral number and τ is a specified small value.

To quantify the benefits of taking into account strain gradient effects within the topological optimization procedure, we describe in the Appendix the procedure using classical homogenization (without strain gradient effects) which are used in the numerical examples of section 5.

3.3. Overall optimization procedure

To summarize, the objective function (overall structural compliance in this work) is computed by solving the mesoscopic problem on a coarse mesh only and the microscopic strain and stress fields (fine scale) are re-localized by means of the localization operators calculated on the unit cells. The design domain is then defined on one unit cell and the optimization problem is solved by using the BESO method as formulated above. The microstructural topology of the representative unit cell is tailored to find the optimal material layout at microscale such that the resulting overall structure has the maximum stiffness within a prescribed amount of material. Finally, the overall multiscale topology optimization procedure for designing the periodic microscopic structures without scale separation using a filter-based homogenization scheme is described as follows.

1. Set a coarse mesh associated with the structure, such that each substructure/unit cell is meshed with the same number of coarse elements. Set another fine mesh related to the microscopic scale to discretize the microstructure of representative unit cell .
2. Assign the pseudo densities (ρ_{min} or 1) to elements in the representative unit cell to construct an initial design before optimization.
3. Perform the microscopic unit cell computations as described in Section 2.2.3.
4. Solve the mesoscopic structure problem as summarized in Section 2.3.
5. Based on the nodal displacement solution from the mesoscopic problem on the coarse mesh, evaluate the local strain field by (35) and the local stress field by (36).
6. Compute the elemental sensitivity number using (49) and modify it by using (50)-(52).
7. Update the structural topology in representative unit cell with (53).
8. Repeat 3-7 until the material constraint V_{req} is satisfied and the convergence criterion (54) is reached.
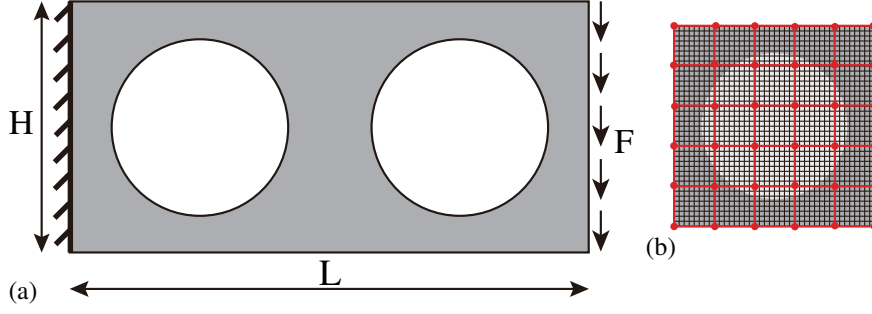
12

Figure 2: Cantilever lattice structure composed of periodic unit cells subjected to distributed force: (a) geometry and boundary conditions of the beam; (b) coarse and fine meshes associated to the unit cell.
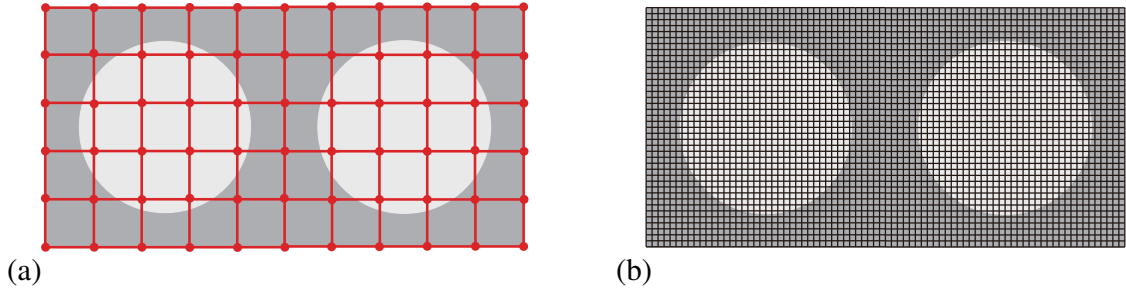

Figure 3: Meshes of the whole structure for computing (a) the mesoscopic problem and (b) the reference solution.

4. Validation of the nonlocal homogenization approach

Even though the nonlocal approach described in section 2 has been validated through various examples in previous works (see e.g. [40]), we present in this section a short validation test for the sake of self-consistency of the paper. The validation test consists in comparing the re-localized field obtained by the present non-local homogenization method on a coarse mesh with a reference solution where all heterogeneities are fully meshed. We consider a structure depicted in Fig. 2 (a). The dimensions of the structure are $L \times H = 200 \times 100$ mm^2. The boundary conditions are described in Fig. 2 (a). The prescribed force is $F = 2$ kN. The unit cell is depicted in Fig. 2 (b). The central hole radius is such that the porosity is equal to 0.6. The material constituting the architectured structure is assumed to be isotropic, with Young's and Poisson's ratio given respectively by $E_m = 1000$ MPa and $v_m = 0.3$. As the topology optimization is more conveniently applied with a regular mesh, the interior of the hole is meshed and associated with a fictive, highly compliant material with Young's and Poisson's ratio given respectively by $E_i = 10^{-6}$ MPa and $v_i = 0.3$. Plane stress is assumed.

The unit cell is discretized with 50×50 regular four-node bilinear elements for the fine scale mesh. A coarse 5×5 mesh is used to construct the localization operators of the nonlocal homogenized model, as described in section 2.2.2. The structure is discretized by a coarse mesh including 10×5 nodes. The reference solution is obtained by discretizing the structure with a regular 100×50 bilinear elements mesh (see Fig. 3 (b). The results are presented in Figs. 4 and
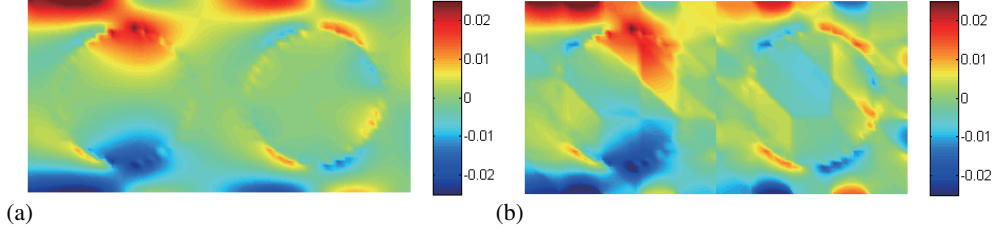
13

Figure 4: (a) Reference solution and (b) re-localized strain field ε_{11} obtained from the nonlocal homogenization method (computed on the coarse mesh).
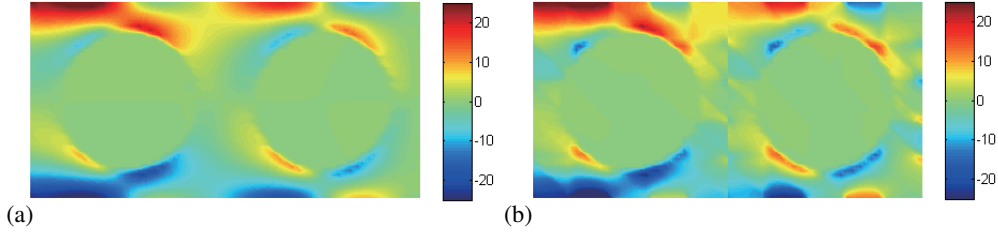

Figure 5: (a) Reference solution and (b) re-localized stress field σ_{11} obtained from the nonlocal homogenization method (computed on the coarse mesh).

5, where the -11 components of the strain and stress fields are plotted for both reference solution and for the re-localized fields obtained by the homogenized model (solved on the coarse mesh). We can note a satisfying agreement between both solutions, demonstrating that the nonlocal homogenized model can be employed for the topology optimization and induces optimal design of lattice structure with versus stiffness while only relying on a coarse mesh. Such procedure will be described in the next section.

5. Numerical examples for topology optimization of periodic lattices taking into account strain gradient

In this section, several numerical examples are presented to demonstrate the capabilities of the proposed topology optimization in a strain gradient context. For all next examples, regular meshes with 4-node elements have been used. The plane stress assumption has been adopted. Here again, to maintain regular meshes during the topology optimization procedure, the regular mesh covers the holes and the related elements are associated to highly compliant properties. The Young's modulus and Poisson's ratio for the material ($\rho_e = 1$) are respectively $E_m = 1000$ MPa and $\nu_m = 0.3$. The fictitious material properties for the holes ($\rho_e = \rho_{min}$) are taken as $E_i = 10^{-6}$ MPa and $\nu_m = 0.3$. At the initiation of the topology optimization, the material distribution is homogeneous with $\rho_e = 1$.

5.1. Cantilever beam with a concentrated load

In this first example, we investigate the topology optimization of a periodic lattice structure subjected to concentrated load. To study the influence of strain gradient effects, the dimensions of the unit cell range from large to small as compared with the dimensions of the structure. The
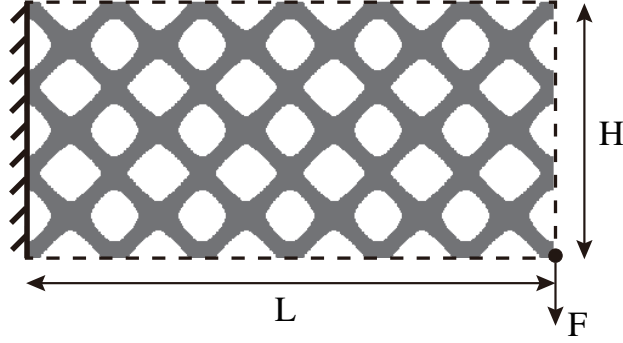
14

Figure 6: Cantilever beam lattice structure composed of periodic microscale unit cells: geometry and boundary conditions.

geometry of the problem is described in Fig. 6. The $x-$ and $y-$ displacements of the left end of the beam are both fixed.

A concentrated force load is applied on the bottom corner of the right end of the domain with a magnitude $F = 100$ N. The aspect ratio of the cantilever beam is chosen as 2 to maximize concentration loads and highlight the strain gradient effects. The dimensions are $L \times H = 2000 \times 1000$ mm^2. The structure is a lattice composed of $N_s = s_1 \times s_2$ unit cells repeated periodically along each space direction, with s_1 and s_2 denoting the number of substructures along $x-$ and $y-$ directions, respectively. A coarse mesh composed of 5×5 elements is associated to the unit cells at the mesoscopic scale. The fine scale mesh on the RVE is composed of 50×50 elements to perform the microscopic unit cell computations. In this example, we keep $s_1 = 2s_2$ (see Fig. 7). 5 cases are studied: (i) $s_1 \times s_2 = 2 \times 1$; (ii) $s_1 \times s_2 = 4 \times 2$; (iii) $s_1 \times s_2 = 8 \times 4$; (iv) $s_1 \times s_2 = 16 \times 8$; (v) $s_1 \times s_2 = 20 \times 10$ (see Fig. 7). These different cases correspond to the following coarse meshes for the structure: (i) 10×5 elements; (ii) 20×10 elements; (iii) 40×20 elements; (iv) 80×40 elements; and (v) 100×50 elements. It is worth reminding that the present homogenization method allows re-localizing the microscale fields. As a result, the total sensitivity number can be reduced by using the local operators in each subdomain. The target volume fraction for the optimized topology of the unit cells is 0.5.

Fig. 7 shows the different optimized topologies of the lattice structure for several number of unit cells along each direction and using on one hand the present method to take into account strain gradient and classical homogenization. Fig. 7 (a) shows the final optimized geometry of the lattice taking into account strain gradient while Fig. 7 (b) shows the final optimized geometry of the lattice without taking into account the strain gradient. Fig. 7 (c) and (d) only shows the optimized geometry of one unit cell for comparison. Along rows (i) - (v), the number of unit cells repeated along each direction is increased and the ratio between the dimensions of the unit cells and the dimensions of the whole structure are decreased. Then for row (i) the scales are not separated while for row (v) the scales can be considered as separated. We can observe from Figs. 7 (i) and (v) that both topological strategies taking into account the strain gradient or not lead to different geometries of unit cells. We can also note that when scales are separated (row (v)), both methods lead to the same topology, which is expected.
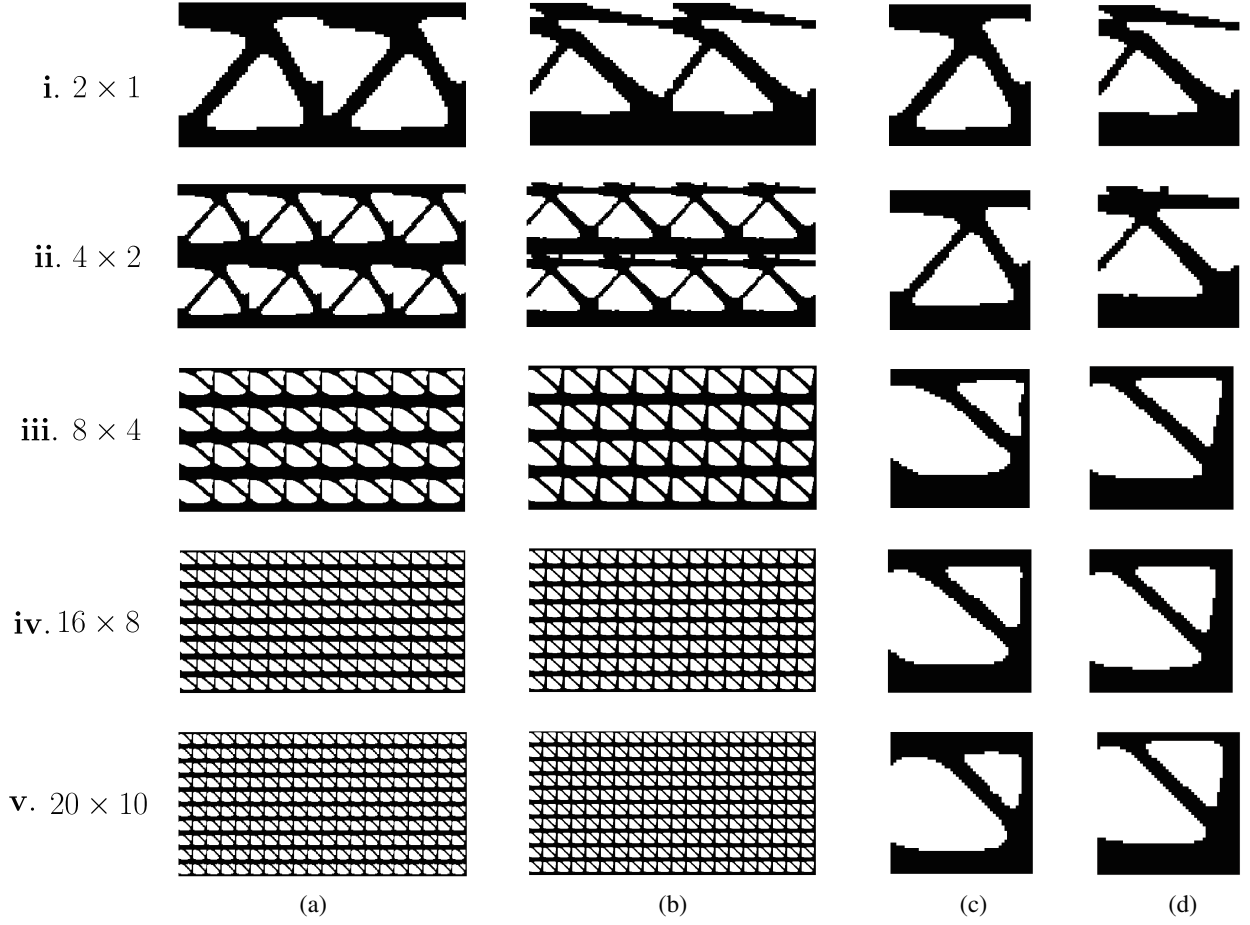
15

Figure 7: Optimized topologies for the cantilever beam lattice structure: columns (a), (b) compare the global lattice topologies when taking into account strain gradient or not in the optimization procedure; columns (c) and (d) show the corresponding unit cell. Rows (i) to (v) correspond to increasing the number of unit cells in the lattice leading to (i) non-separated scales; (v) separated scales.

To quantify the gains obtain by the present method, in Fig. 8, we compare the compliances for optimized geometries of the lattice when the strain gradient is taken into account or not. We can see that using the present nonlocal homogenization method, the obtained resulting compliance is lower than using classical homogenization (then ignoring strain gradient effects), inducing a significant gain in the resulting stiffness of the lattice. We also note that when the number of unit cells is large, then both methods lead to the same compliance, which is also consistent as the scale are in this case separated.

In this work, standard BESO method is adopted to solve the proposed optimization problem. This method updates the topology of the RVE by removing certain amount of material step by step, in order to finally meet the volume constraint. Normally, the evolutionary volume ratio is set to 2% [8, 41] which means that 2% solid elements within the design domain are deleted from the previous design iteration. This value cannot be too large to avoid accidentally deleting too many solid elements at each iteration [8, 41]. However, if it is too small, more iterations are needed
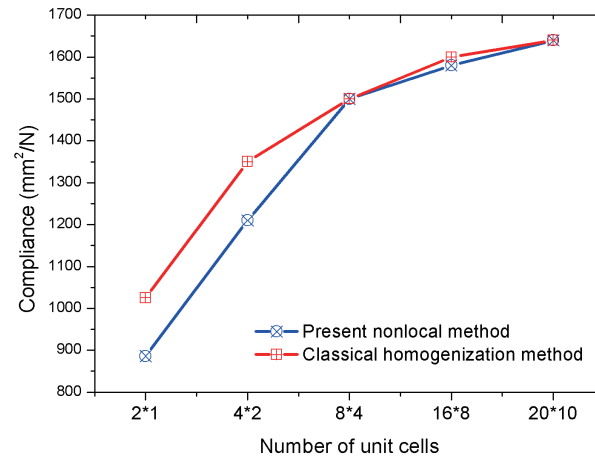
Figure 8: Compliance obtained by topological optimization when taking into strain gradient effects (blue curve) and without taking into account strain gradient (red curve). Results are plotted as a function of the number of unit cells, and large number of unit cells leads to scale separation.
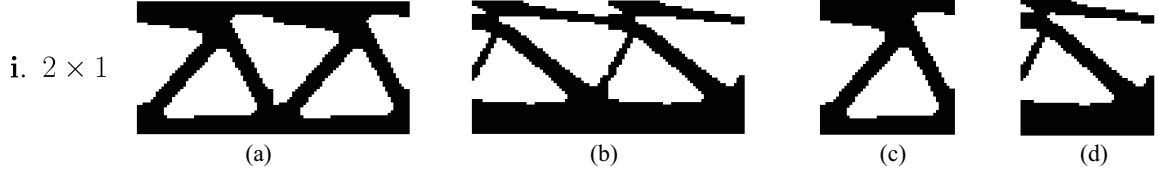
i. 2×1

          (a)   (b)   (c)   (d)

Figure 9: Optimized topologies for the cantilever beam lattice structure using small evolutionary volume ratio c_{er}: columns (a), (b) compare the global lattice topologies when taking into account strain gradient or not in the optimization procedure; columns (c) and (d) show the corresponding unit cell.
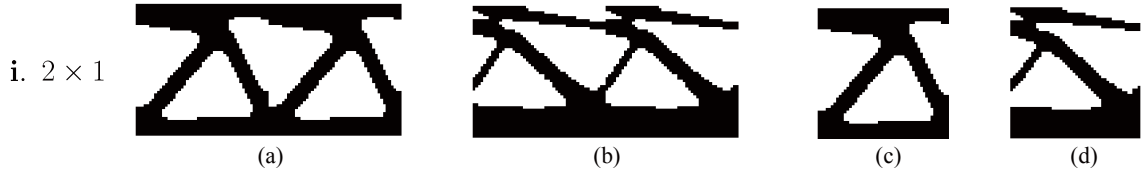
i. 2×1

          (a)   (b)   (c)   (d)

Figure 10: Optimized topologies for the cantilever beam lattice structure using small τ: columns (a), (b) compare the global lattice topologies when taking into account strain gradient or not in the optimization procedure; columns (c) and (d) show the corresponding unit cell.

from the initial design to reach the final volume constraint. Taking the case (i) in this numerical experiment as an example, when we set the evolutionary volume ratio as 1%, the different optimized topologies of the lattice structure using the present method and classical homogenization are shown in Fig. 9. We can see that there is no noticeable difference of the topologies in Fig. 9 and Fig. 7 row (i). However, the solution in Fig. 9 requires twice the number of iterations since a small value of evolutionary volume ratio is adopted. In addition, a specified small number τ given in Eq. (54) is used to stop the optimization procedure when the volume constraint is satisfied and objective function is kept the constant. In this case, when we set a smaller τ as 0.1%, the optimized topologies for the cantilever beam lattice structure are shown in Fig. 10. We can see no change in the topology and thus no sensitivity on τ in this case.

As an illustration, we depict in Fig. 11 the evolution of the microstructure topology for the case of non-separated scales (1×2 unit cells) using the present homogenization method for taking into account strain gradient effects. These evolutions correspond to different iterations in the topology optimization procedure. It is worth reminding that the present optimization method is able to start from an initial guess without holes, which is not the case in most multiscale optimization methods available which require one or several holes for initiating the procedure.

It is noted that any volume fraction constraint can be selected by the designer in the present optimization procedure. In this example, when we set the volume fraction value to 0.6, the compliances for optimized geometries of the lattice when the strain gradient is taken into account or not are compared in Fig. 12. We can see that using the present nonlocal homogenization method, the obtained resulting compliance in this case is also lower than using classical homogenization, resulting in a higher stiffness of the structure. In addition, when the number of unit cells is large, then both methods lead to the same compliance, which is also consistent with the case when the volume constraint is set as 0.5.
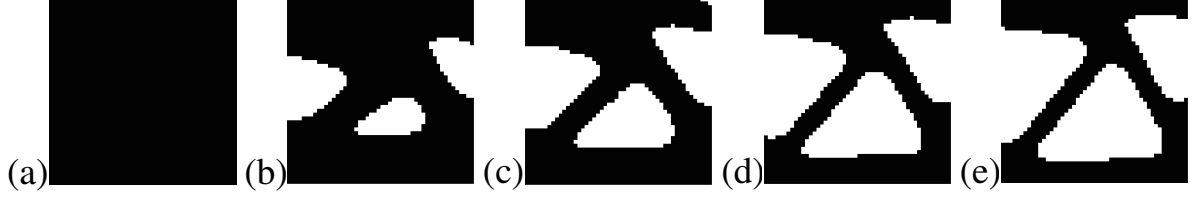
18

Figure 11: Evolution of the optimized topology of the unit cell for the cantilever beam lattice with $N_s = 2 \times 1$ periodic cells: (a) iteration 0; (b) iteration 10; (c) iteration 20; (d) iteration 30; (e) iteration 40 (final topology).
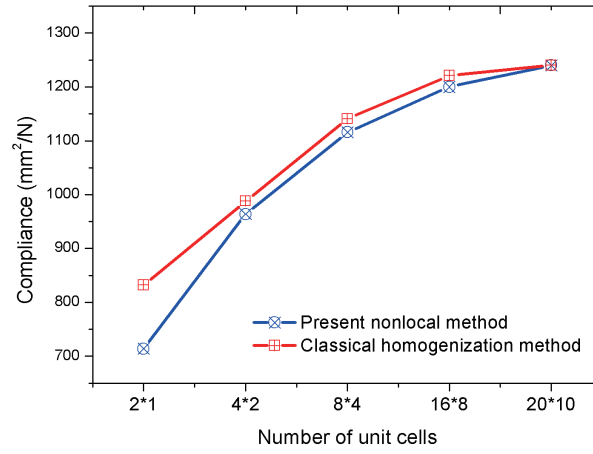

Figure 12: Compliance obtained by topological optimization when taking into strain gradient effects (blue curve) and without taking into account strain gradient (red curve). Results are plotted as a function of the number of unit cells, and large number of unit cells leads to scale separation.
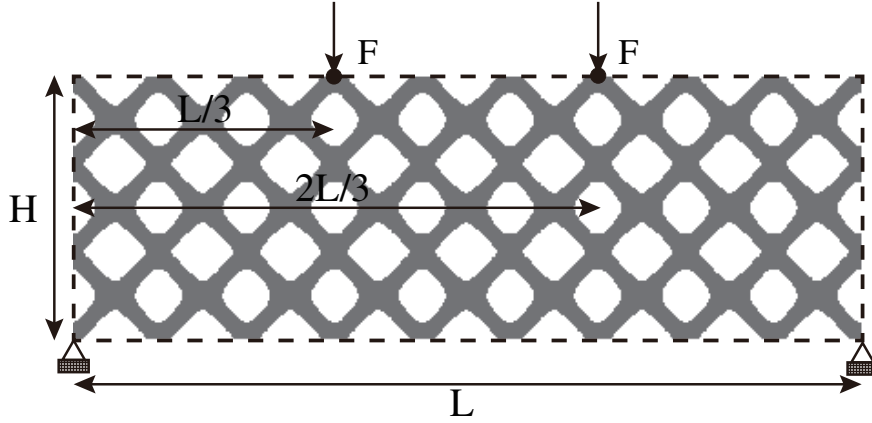
19

Figure 13: Four-point bending beam lattice structure composed of periodic unit cells: geometry and boundary conditions.

5.2. Four-point bending lattice structure

In this second example, a lattice structure is subjected to four-point bending. The geometry of the problem is depicted in Fig.13. The dimensions of the lattice structure along $x-$ and $y-$ are $L = 3000$ mm and $H = 1000$ mm, respectively. The left and right bottom corner nodes are fixed in both $x-$ and $y-$ directions. On the upper end concentrated forces are applied (see Fig. 13).

The loading force is taken as $F = 100$ N. The mesh used for the fine scale within the RVE is composed of 40×40 elements. The target volume fraction for the optimized topology of unit cells is 0.6. As in the previous example, the number of unit cells composing the lattice is varied to study the effects of the scale separation. In this example, larger number of unit cells was adopted to explain that the number of involved degrees of freedom in the proposed method is significantly reduced against direct meshing. Then, the following numbers of unit cells along each directions are investigated: (i) 3×1; (ii) 6×2; (iii) 15×5; (iv) 30×10; and (v) 48×16. The corresponding coarse meshes are composed of respectively (i) 15×5 elements; (ii) 30×10 elements; (iii) 75×25 elements; (iv) 150×50 elements and (v) 240×80 elements. It is worth noting that in the last case, solving the topology optimization problem with a direct meshing of the microstructure would involve 2,462,722 degrees of freedom. Using the present technique, the topological optimization procedure only uses the nodes of the coarse mesh through the homogenized nonlocal model and then drastically reduces the computational costs. For the last case, the coarse mesh only contains 39,042 degrees of freedom.

As in the previous example, Fig. 14 shows the different optimized topologies of the lattice structure for several number of unit cells along each direction and using on one hand the present method to take into account strain gradient and classical homogenization. We can observe from Figs. 14 (i) and (v) the different topologies when strain gradient is taken into account or not. Here again, when scales are separated (row (v)), both methods lead to the same topology. We compare the compliances for optimized geometries of the lattice when the strain gradient is taken into account or not in Fig. 15. Using the present nonlocal homogenization method, the obtained resulting compliance is here again lower than using classical homogenization (then ignoring strain gradient effects), inducing a gain in the resulting stiffness (or a decrease in the compliance) of the
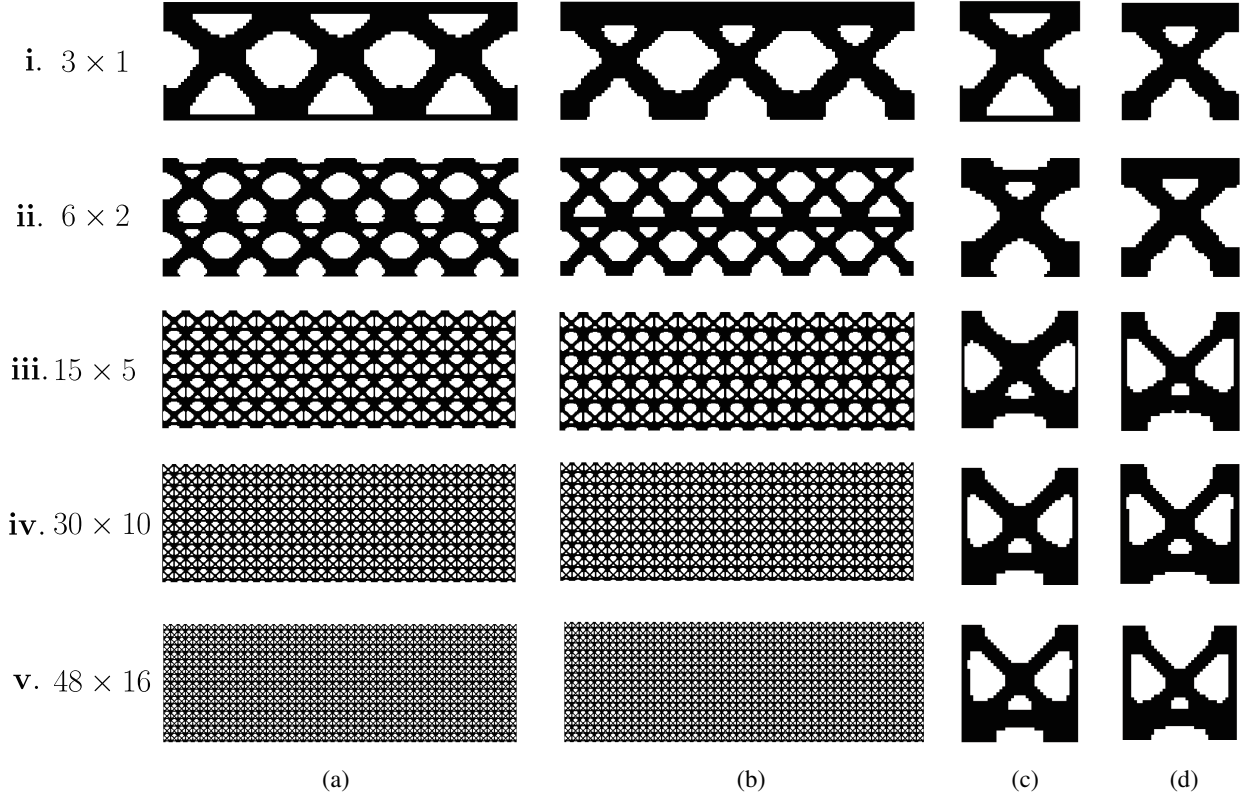
Figure 14: Optimized topologies for the four-point bending beam lattice structure: columns (a), (b) compare the global lattice topologies when taking into account strain gradient or not in the optimization procedure; columns (c) and (d) show the corresponding unit cell. Rows (i) to (v) correspond to increasing the number of unit cells in the lattice leading to (i) non-separated scales; (v) separated scales.

lattice. The evolution of the topology of the unit cell for the case (v) is shown in Fig. 16. The whole multiscale topological design process converges after 34 iterations in this case. These results show that when scales are not separated, the present topology optimization based on a homogenization method taking into account strain gradient brings an added value by inducing a larger stiffness of the final lattice.

6. Conclusions

In this paper, we have presented a topological optimization method for lattice structures in the case when scales are not separated, i.e. when the characteristic dimensions of the unit cells are not much lower than the dimensions of the structure. This case can occur in many situations, as the additive manufacturing processes can lead to very large times to produce the lattice structures if the unit cell dimensions are very small. To avoid solving the full problem involving all degrees of freedom and possibly large computational times within topology optimization framework, we use a strain gradient homogenization method for each periodic cell. The strain gradient homogenization method is based on the filter based homogenization as proposed in [40]. In this technique, the total number of degrees of freedom in the topological optimization problem is reduced by using
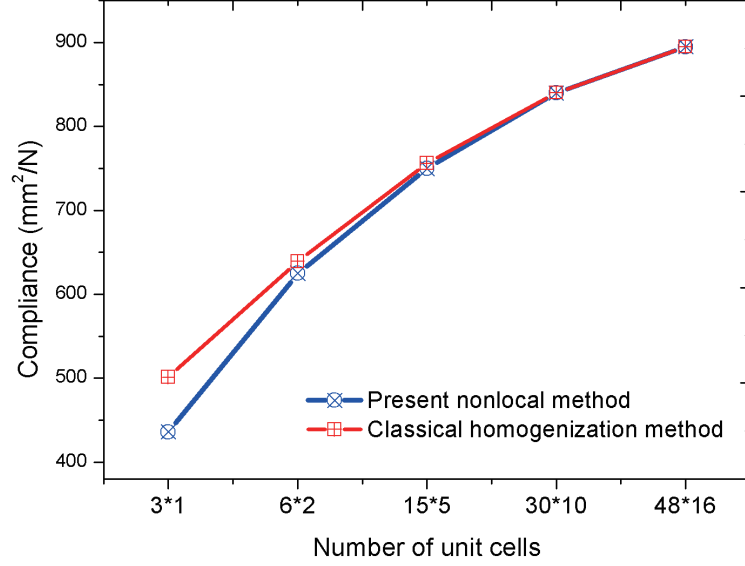
21

Figure 15: Compliance obtained by topological optimization when taking into strain gradient effects (blue curve) and without taking into account strain gradient (red curve) for the four-point bending beam. Results are plotted as a function of the number of unit cells, and large number of unit cells leads to scale separation.
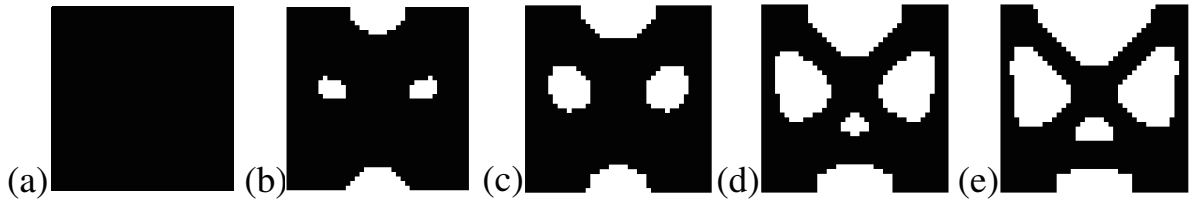

Figure 16: Evolution of the optimized topology of the unit cell for the four-point bending beam with $N_s = 48 \times 16$ periodic cells: (a) iteration 0; (b) iteration 5; (c) iteration 10; (d) iteration 20; (e) iteration 34 (final topology).

a coarse mesh which parameterizes the local fields. We have applied the proposed method to lattice structures submitted to different loads, with different number of periodic cells, from low to large, to show the influence of the size effects. When size effects are pronounced, i.e. when the dimensions of the elementary cells are not too small as compared with the dimensions of the structure, we show that the present method, leads to a topology inducing a higher stiffness of the structure (lower compliance) as compared with classical homogenization method.

Acknowledgements

7. Appendix: topological optimization with classical homogenization (no strain gradient effects)

To quantify the benefits of taking into account strain gradient effects within the topological optimization procedure, we describe here the procedure using classical homogenization (without strain gradient effects) which is used in the numerical example in section 5. If no strain gradient effects are included, the optimization problem is solved using the classical homogenization method by assuming the separation of scales. The effective constitutive relationship is obtained by subjecting the unit cell to uniform elementary strain fields (see e.g. [28]). This effective or homogenized behavior is used to solve the mesoscopic structure problem at the same coarse mesh as in the framework of nonlocal filter-based homogenization method. Therefore, a similar structural stiffness maximization problem using the classical homogenization method can be formulated as

$$
\begin{aligned}
\min_{\{\boldsymbol{\rho}^{(1)},\ldots,\boldsymbol{\rho}^{(N_s)}\}} \; &: \; f_{\mathrm{c}}(\boldsymbol{\rho},\hat{\mathbf{u}}) = \hat{\mathbf{F}}^T \hat{\mathbf{u}} \\
\text{subject to} \; &: \; \hat{\mathbf{K}}' \hat{\mathbf{u}} = \hat{\mathbf{F}} \\
&: \; V(\boldsymbol{\rho}) = N_s \sum \rho_e^{(k)} v_e^{(k)} = V_{\mathrm{req}} \\
&: \; \rho_e^{(1)} = \cdots = \rho_e^{(N_s)}, \; e = 1,\ldots,N_e \\
&: \; \rho_e^{(k)} = \rho_{min} \text{ or } 1, \; e = 1,\ldots,N_e
\end{aligned} \tag{55}
$$

where f_{c} is the compliance functional, and $\hat{\mathbf{K}}'$ is the global stiffness matrix which is defined as:

$$
\hat{\mathbf{K}}' = \sum_k \int_{\hat{\Omega}^k} \mathbf{B}^T(x) \overline{\mathbf{C}} \mathbf{B}(x) d\Omega, \tag{56}
$$

where $\mathbf{B}$ is the matrix of the shape function derivatives, and $\overline{\mathbf{C}}$ denotes the matrix form of the effective elasticity tensor $\overline{\mathbb{C}}$ obtained from the classical homogenization by prescribing unitary constant strain fields by

$$
\overline{\mathbb{C}} = \langle \mathbb{A}(\mathbf{x})\mathbb{C}(\mathbf{x}) \rangle, \tag{57}
$$

where $\mathbb{A}(x)$ is the localization tensor such that $\boldsymbol{\varepsilon}(\mathbf{x}) = \mathbb{A}(\mathbf{x}) : \overline{\boldsymbol{\varepsilon}}$, where $\overline{\boldsymbol{\varepsilon}}$ denotes a constant macroscopic strain field prescribed over the unit cell. Therefore, the re-localized strain and stress fields in this scheme are denoted by $\boldsymbol{\varepsilon}^{cla}(x)$ and $\boldsymbol{\sigma}^{cla}(x)$ and are respectively obtained using the localization tensor $\mathbb{A}(x)$ within each unit cell/substructure as follows

$$\boldsymbol{\varepsilon}^{cla}(\boldsymbol{x}) = \mathbb{A}(\boldsymbol{x}) : \hat{\boldsymbol{\varepsilon}}(\boldsymbol{x}) \tag{58}$$

and

$$\boldsymbol{\sigma}^{cla}(\boldsymbol{x}) = \mathbb{C}(\boldsymbol{x}) : \mathbb{A}(\boldsymbol{x}) : \hat{\boldsymbol{\varepsilon}}(\boldsymbol{x}); \tag{59}$$

where $\hat{\boldsymbol{\varepsilon}}(\boldsymbol{x})$ is the strain field obtained from the displacement solution at the coarse mesh, calculated by solving the mesoscopic problem via effective or homogenized constitutive behavior. Correspondingly, the elemental sensitivity number in this scheme defined as the change of the structural compliance or total strain energy since the removal of the $e-$th element in each substructure, i.e. the summation of the elemental strain energy in all substructures can be formulated as

$$\alpha_e^{cla} = \begin{cases} \sum_{k=1}^{N_s} \int_{\Omega_e^k} \boldsymbol{\sigma}^{cla}(\boldsymbol{x}) \boldsymbol{\varepsilon}^{cla}(\boldsymbol{x}) d\Omega_e^k, & \text{for } \rho_e^{(k)} = 1 \\ 0, & \text{for } \rho_e^{(k)} = \rho_{min}. \end{cases} \tag{60}$$

The same overall optimization procedure as described in section 3.3 is adopted with the classical homogenization solution with the following changes: (i) the microscopic unit cell computations in step 3 are performed in the context of classical homogenization with separation of scales to obtain the localization tensor $\mathbb{A}$ and the homogenized elasticity tensor $\overline{\mathbb{C}}$; (ii) the mesoscopic structure problem is solved based on the above homogenized elasticity tensor $\overline{\mathbb{C}}$; (iii) the re-localized strain and stress fields at all substructures/unit cells are computed by (58) and (59), respectively, and the final elemental sensitivity number is obtained according to (60). The detailed optimization procedure based on the classical homogenization can be found in [48].

References

[1] X. Wang, S. Xu, S. Zhou, W. Xu, M. Leary, P. Choong, M. Qian, M. Brandt, Y. M. Xie, Topological design and additive manufacturing of porous metals for bone scaffolds and orthopaedic implants: a review, Biomaterials 83 (2016) 127–141.

[2] M. P. Bendsøe, N. Kikuchi, Generating optimal topologies in structural design using a homogenization method, Computer Methods in Applied Mechanics and Engineering 71 (2) (1988) 197–224.

[3] G. Allaire, Shape optimization by the homogenization method, Vol. 146, Springer Science & Business Media, 2012.

[4] M. P. Bendsøe, Optimal shape design as a material distribution problem, Structural Optimization 1 (4) (1989) 193–202.

[5] M. Zhou, G. I. N. Rozvany, The coc algorithm, part ii: Topological, geometrical and generalized shape optimization, Computer Methods in Applied Mechanics and Engineering 89 (1-3) (1991) 309–336.

[6] Y. M. Xie, G. P. Steven, A simple evolutionary procedure for structural optimization, Computers and Structures 49 (5) (1993) 885–896.

[7] Y. M. Xie, G. P. Steven, Evolutionary Structural Optimization, Springer-Verlag, London, 1997.

[8] X. Huang, M. Xie, Evolutionary topology optimization of continuum structures: methods and applications, John Wiley & Sons, 2010.

[9] J. A. Sethian, A. Wiegmann, Structural boundary design via level set and immersed interface methods, Journal of Computational Physics 163 (2) (2000) 489–528.

[10] M. Y. Wang, X. Wang, D. Guo, A level set method for structural topology optimization, Computer Methods in Applied Mechanics and Engineering 192 (1-2) (2003) 227–246.

[11] G. Allaire, F. Jouve, A. M. Toader, Structural optimization using sensitivity analysis and a level-set method, Journal of Computational Physics 194 (1) (2004) 363–393.

[12] O. Sigmund, Materials with prescribed constitutive parameters: An inverse homogenization problem, International Journal of Solids and Structures 31 (17) (1994) 2313–2329.

[13] X. Huang, A. Radman, Y. M. Xie, Topological design of microstructures of cellular materials for maximum bulk or shear modulus, Computational Materials Science 50 (6) (2011) 1861–1870.

[14] L. Xia, P. Breitkopf, Design of of materials using topology optimization and energy-based homogenization approach in matlab, Structural and Multidisciplinary Optimization 52 (6) (2015b) 1229–1241.

[15] O. Sigmund, S. Torquato, Design of materials with extreme thermal expansion using a three-phase topology optimization method, Journal of the Mechanics and Physics of Solids 45 (6) (1997) 1037–1067.

[16] L. Gibiansky, O. Sigmund, Multiphase composites with extremal bulk modulus, Journal of the Mechanics and Physics of Solids 48 (3) (2000) 461–498.

[17] E. Andreassen, J. Jensen, Topology optimization of periodic microstructures for enhanced dynamic properties of viscoelastic composite materials, Structural and Multidisciplinary Optimization 49 (5) (2014) 695–705.

[18] W. Chen, S. Liu, Topology optimization of microstructures of viscoelastic damping materials for a prescribed shear modulus, Structural and Multidisciplinary Optimization 50 (2) (2014) 287–296.

[19] X. Huang, S. Zhou, G. Sun, G. Li, Y. M. Xie, Topology optimization for microstructures of viscoelastic composite materials, Computer Methods in Applied Mechanics and Engineering 283 (2015) 503–516.

[20] Y. Zhu, Z.-P. Wang, L. H. Poh, Auxetic hexachiral structures with wavy ligaments for large elasto-plastic deformation, Smart Materials and Structures 27 (5) (2018) 055001.

[21] A. Clausen, F. Wang, J. S. Jensen, O. Sigmund, J. A. Lewis, Topology optimized architectures with programmable poisson's ratio over large deformations, Advanced Materials 27 (37) (2015) 5523–5527.

[22] D. Da, J. Chen, X. Cui, G. Li, Design of materials using hybrid cellular automata, Structural and Multidisciplinary Optimization 56 (1) (2017) 131–137.

[23] Y. M. Xie, X. Yang, J. Shen, X. Yan, A. Ghaedizadeh, J. Rong, X. Huang, S. Zhou, Designing orthotropic materials for negative or zero compressibility, International Journal of Solids and Structures 51 (23-24) (2014) 4038–4051.

[24] Z.-P. Wang, L. H. Poh, J. Dirrenberger, Y. Zhu, S. Forest, Isogeometric shape optimization of smoothed petal auxetic structures via computational periodic homogenization, Computer Methods in Applied Mechanics and Engineering 323 (2017) 250–271.

[25] Y. Noguchi, T. Yamada, K. Izui, S. Nishiwaki, Optimum design of an acoustic metamaterial with negative bulk modulus in an acoustic-elastic coupled system using a level set–based topology optimization method, International Journal for Numerical Methods in Engineering 113 (8) (2018) 1300–1339.

[26] S. Nanthakumar, T. Lahmer, X. Zhuang, H. S. Park, T. Rabczuk, Topology optimization of piezoelectric nanostructures, Journal of the Mechanics and Physics of Solids 94 (2016) 316–335.

[27] S. Nanthakumar, X. Zhuang, H. S. Park, T. Rabczuk, Topology optimization of flexoelectric structures, Journal of the Mechanics and Physics of Solids 105 (2017) 217–234.

[28] J. C. Michel, H. Moulinec, P. Suquet, Effective properties of composite materials with periodic microstructure: A computational approach, Computer Methods in Applied Mechanics and Engineering 172 (1-4) (1999) 109–143.

[29] L. Xia, P. Breitkopf, Concurrent topology optimization design of material and structure within fe^2 nonlinear multiscale analysis framework, Computer Methods in Applied Mechanics and Engineering, 278 (2014a) 524–542.

[30] L. Xia, P. Breitkopf, Multiscale structural topology optimization with an approximate constitutive model for local material microstructure, Computer Methods in Applied Mechanics and Engineering, 286 (2015a) 147–167.

[31] D. C. Da, X. Y. Cui, K. Long, G. Y. Li, Concurrent topological design of composite structures and the underlying multi-phase materials, Computers and structures 179 (1) (2017) 1–14.

[32] L. Xia, D. Da, J. Yvonnet, Topology optimization for maximizing the fracture resistance of quasi-brittle composites, Computer Methods in Applied Mechanics and Engineering 332 (2017) 234–254.

[33] D. Da, J. Yvonnet, L. Xia, L. Guangyao, Topology optimization of particle-matrix composites for optimal fracture resistance taking into account interfacial damage, International Journal for Numerical Methods in Engineering (2018) 1–23.

[34] M. G. Geers, V. G. Kouznetsova, W. Brekelmans, Multi-scale computational homogenization: Trends and challenges, Journal of Computational and Applied Mathematics 234 (7) (2010) 2175–2182.

[35] R. Peerlings, R. De Borst, W. Brekelmans, J. De Vree, I. Spee, Some observations on localisation in non-local and gradient damage models, European Journal of Mechanics A/Solids 15 (1996) 937–954.

[36] V. Kouznetsova, M. G. Geers, W. Brekelmans, Multi-scale constitutive modelling of heterogeneous materials with a gradient-enhanced computational homogenization scheme, International Journal for Numerical Methods in Engineering 54 (8) (2002) 1235–1260.

[37] A. C. Eringen, D. G. Edelen, On nonlocal elasticity, International Journal of Engineering Science 10 (1972) 233–248.

[38] J. Yvonnet, G. Bonnet, A consistent nonlocal scheme based on filters for the homogenization of heterogeneous linear materials with non-separatd scales, International Journal of Solids and Structures 51 (2014) 196–209.

[39] J. Yvonnet, G. Bonnet, Nonlocal/coarse-graining homogenization of linear elastic media with nonseparated scales using least-square polynomial filters, International Journal for Multiscale Computational Engineering 51 (2014) 196–209.

[40] A. Tognevi, M. Guerich, J. Yvonnet, A multi-scale modeling method for heterogeneous structures without scale separation using a filter-based homogenization scheme, International Journal for Numerical Methods in Engineering 108 (1) (2016) 3–25.

[41] X. Huang, Y. M. Xie, Convergent and mesh-independent solutions for the bi-directional evolutionary structural optimization method, Finite Elements in Analysis and Design 43 (14) (2007) 1039–1049.

[42] Y. M. Xie, Z. H. Zuo, X. Huang, J. H. Rong, Convergence of topological patterns of optimal periodic structures under multiple scales, Structural and Multidisciplinary Optimization 46 (2012) 41–50.

[43] Z. H. Zuo, X. Huang, X. Yang, J. H. Rong, Y. M. Xie, Comparing optimal material microstructures with optimal periodic structures, Computational Materials Science 69 (2013) 137–147.

[44] W. Zhang, S. Sun, Scale-related topology optimization of cellular materials and structures, International Journal for Numerical Methods in Engineering 68 (2006) 993–1011.

[45] J. Alexandersen, B. S.Lazarov, Topology optimisation of manufacturable microstructural details without length scale separation using a spectral coarse basis preconditioner, Computer Methods in Applied Mechanics and Engineering 290 (2015) 156–182.

[46] D. N. Chu, Y. M. Xie, A. Hira, G. P. Steven, Evolutionary structural optimization for problems with stiffness constraints, Finite Elements in Analysis and Design 43 (14) (2007) 1039–49.

[47] O. Sigmund, A 99 line topology optimization code written in matlab, Structural and Multidisciplinary Optimization 21 (2) (2001) 120–127.

[48] D. Da, J. Yvonnet, L. Xia, G. Li, Size effects analysis in topology optimization for periodic structures using the classical homogenization, Submitted for publication.